Alleviating Anisotropic Volume Variation at Comparable Li Utilization during Cycling of Ni-Rich, Co-Free Layered Oxide Cathode Materials

Published as part of The Journal of Physical Chemistry virtual special issue "Esther Sans Takeuchi Festschrift".

Damian Goonetilleke, Felix Riewald, Aleksandr O. Kondrakov, Jürgen Janek, Torsten Brezesinski, and Matteo Bianchini*

ABSTRACT: Driven by demand for greater energy densities, Ni-rich cathode materials, such as lithium nickel cobalt manganese (NCM) and nickel cobalt aluminum (NCA) oxides, with compositions approaching the lithium nickel oxide ($LiNiO_2$) end-member have been investigated intensively. While such compositions are targeted assuming the redox activity of nickel will lead to higher capacities, the role of even small amounts of Mn and Co in these systems is of great importance. To raise considerations about the role of Mn and Co, *operando* X-ray diffraction has been used to resolve the structure−electrochemistry relationships in a series of Ni-rich NMX ($LiNi_{1-y}Mn_yO_2$, y = 0.25, 0.17, 0.10, 0.05) cathode materials. To ensure a meaningful comparison, the upper cutoff potential was varied as a function of the Mn content in the material to ensure comparable states of delithiation and thereby provide a capacity-normalized comparison of the structural evolution. During the first cycle all materials deliver a specific charge capacity exceeding 230 mAh g^{-1}, corresponding to a residual Li content of $x(Li) \approx 0.15$, and exhibit a structural evolution free of any first-order phase transitions. Monitoring the structural parameters of the materials during cycling shows that Mn substitution substantially reduces the magnitude of expansion/contraction of lattice parameters even when comparable amounts of Li are removed from the structure and more significantly also reduces the anisotropy of the volume changes. Thus, these Co-free, Ni-rich materials hold promise as high-capacity cathodes with good structural and mechanical stability.

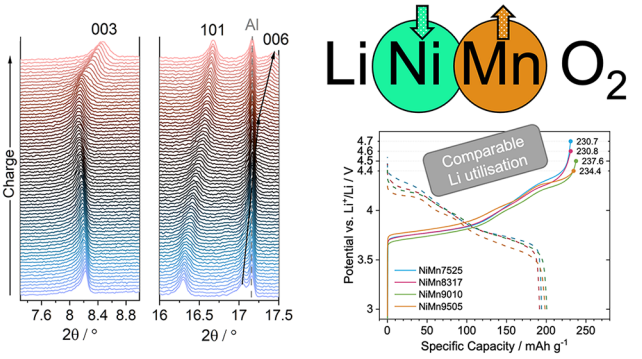

■ INTRODUCTION

The rapid transition toward practical and accessible electromobility has been driven by improvements in lithium-ion batteries (LIBs). These devices enable high energy and power densities with respect to both volume and weight compared to other secondary energy storage systems. For high energy density applications, the cathode material is most commonly based on a layered transition-metal oxide, such as $LiNi_aCo_bMn_cO_2$ (NCM) or $LiNi_aCo_bAl_cO_2$ (NCA) ($a + b + c = 1$).[1−3] The combination of transition metals to produce Ni-rich layered oxides has brought significant advancements to the energy density and structural stability achievable in this class of materials.[4,5] It is generally concluded that a higher Ni content improves energy density due to its high electrochemical redox activity; Co is beneficial to rate capability and is important during synthesis to form a well-ordered layered structure, while Mn improves structural stability and raises the average voltage without partaking in the electrochemical redox reaction. To improve specific capacity, the nickel content has progressively increased in these materials. Meanwhile, issues with the sourcing of cobalt, due to its toxicity and scarcity, have also driven the development of Co-free cathode materials.[6−8] Additionally, several recent studies have questioned the necessity of cobalt in Ni-rich cathode materials for applications requiring high energy density, and comparable performance and structural stability can be achieved using other substituent elements.[9−12] In the O3-type layered structure, depicted in the inset of Figure 1, Li ions occupy the 3*a* octahedral interstitial sites of the oxygen sublattice, consisting of a cubic close-

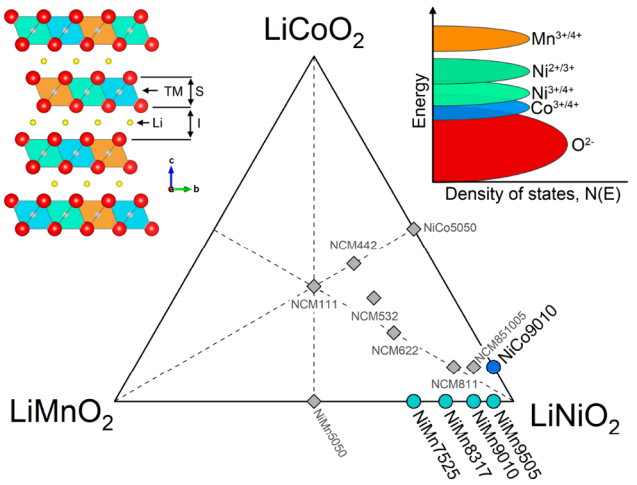

Figure 1. Phase diagram of the $LiNiO_2$–$LiMnO_2$–$LiCoO_2$ system. Blue dots highlight the materials studied here. Left inset: illustration of the O3-type layered structure. I and S represent the interlayer thickness (interslab) and TM layer thickness (slab), respectively. Right inset: schematic depicting the redox energies of Ni, Mn, and Co species relative to the O^{2-}:2p band.

packed (ccp) array of oxygen ions (6*c* sites), while TM cations are situated alternatingly in the 3*b* sites.[13]

The ternary cathode phases $LiCoO_2$ (LCO) and $LiNiO_2$ (LNO) have each been studied extensively and present their own favorable properties and also drawbacks.[14−17] The small ionic radius of Li (0.76 Å) prevents many elements (0.5−0.7 Å) from readily crystallizing into layered $LiMO_2$ structures ($R\bar{3}m$ space group) when prepared via solid-state synthesis, with the exception of the $LiCoO_2$, $LiNiO_2$, and $LiVO_2$ phases.[18−20] In contrast, $LiMnO_2$ generally crystallizes with an orthorhombic structure (*Pmmm*).[21] The family of Mn-based spinel materials has also been investigated thoroughly; however, the comparatively low practical specific capacity (≈120 mAh g^{-1}, compared to >200 mAh g^{-1} for layered materials) has prevented its wider adoption.[22,23] $LiMnO_2$ with a layered structure had also been reported and was obtained via ion exchange from the sodium analogue ($NaMnO_2$).[24−26] However, several studies revealed a transition to the spinel structure after successive (de)intercalations.[27,28] While $LiCoO_2$ initially enabled the commercialization of the contemporary LIB (graphite ‖ $LiCoO_2$),[29] complete utilization of the Li content available in the cathode could not be realized due to oxygen release at high levels of delithiation. This can be explained by considering the electronic structure of the material, where the Co^{3+}/Co^{4+} redox couple overlaps with the band of the O^{2-}:2p (see Figure 1), explaining the oxygen activity at high potential in this material. The overlap of the Ni^{3+}/Ni^{4+} redox couple in $LiNiO_2$ is much less pronounced, and the Mn^{3+}/Mn^{4+} band expected in $LiMnO_2$ is situated significantly higher than the O^{2-}:2p band, enabling high oxidation states to be achieved without the loss of lattice oxygen.[19] Thus, $LiNiO_2$ can be cycled to higher potentials without encountering oxygen redox (≈230 mAh g^{-1} at 4.3 V).[30] However, in practice modern $LiCoO_2$ cells are typically operated up to a lower cutoff voltage to avoid fast capacity fading caused by excessive mechanical degradation (≈165 mAh g^{-1} at 4.35 V).[31] As discussed above, the observed electrochemical behavior and associated phase transitions in ternary layered oxide phases can be related to the changing electronic configuration of the active transition-metal ions during delithiation.[32−34] Hence, the introduction of substituent atoms to produce more complex quaternary (e.g., Li−Ni−Mn−O) or quintenary (e.g., Li−Ni−Mn−Co−O) phases should also be expected to influence the electronic configuration of adjacent metal ions and thereby influence the potential at which a given cation redox couple is active.[35−37] The preparation of solid solutions of these ternary layered oxides allows for the redox activity and advantageous physical properties of the basic ternary phases to be harnessed in a homogeneous phase, as shown in Figure 1. The composition of the resulting solid solutions is also consequential for the potential at which each TM redox couple is active. In a pure ternary layered oxide composition, all TM sites experience the same electric crystal field, and the covalency of the TM−O bond in each octahedron is also identical. However, in a solid solution, substitution at the TM site influences the interaction of neighboring cations with their surrounding oxygen octahedra. Thus, subtle differences in the redox behavior are observed in quaternary and higher phases compared to the ternary phases.

Studying the dynamic behavior of cathode materials during charge and discharge has been achieved via a variety of advanced *in situ* or *operando* characterization techniques, ranging from X-ray or neutron scattering, tomography, and spectroscopy to microscopy via electrons, light, or scanning probe and other physical techniques such as monitoring pressure or gas evolution.[38−44] Among these, the use of X-ray diffraction (XRD) to investigate the structural evolution of the active materials in real time (*operando*) has been widely adopted, largely because of the greater accessibility of synchrotron sources and ease of construction of proper windowed coin cells for researchers.[45,46] Simultaneous advancements in the resolution and intensity of lab X-ray sources now also allow for such studies to be undertaken at researcher's home institutions.[47]

This study examines the structure−electrochemistry relationships in a series of Ni-rich NMX ($LiNi_{1-y}Mn_yO_2$, y = 0.25, 0.17, 0.10, 0.05) cathode materials with comparison to $LiNi_{0.9}Co_{0.1}O_2$. To ensure the observed structural evolution is comparable between the different materials, the applied upper cutoff potentials have been varied to control the degree of delithiation. *Operando* XRD confirms the absence of any first-order phase transitions in all of the materials investigated when the different materials are subjected to commensurate levels of Li utilization (x(Li) ≈ 0.15, q_{ch} > 230 mAh g^{-1}).

EXPERIMENTAL SECTION

Material Synthesis. A series of Ni-rich cathode materials were synthesized from coprecipitated hydroxide precursors of the appropriate stoichiometry: $Ni_{1-y}Mn_y(OH)_2$ (y = 0.25, 0.17, 0.10, 0.05) and $Ni_{0.9}Co_{0.1}(OH)_2$ (BASF SE); $LiOH{\cdot}H_2O$ (BASF SE) was used as the lithium source, with a stoichiometric lithium excess n(TM):n(Li) = 1:1.01. The hydroxide precursors were mixed using a laboratory blender (Kinematica AG) to ensure homogeneity and transferred to an alumina crucible. The precursor mixtures were heated under O_2 flow to desired annealing temperatures ranging from 700 to 900 °C with a ramp rate of 3 °C min^{-1} and held for 6 h.

Electrode Preparation. Electrodes for electrochemical characterization were prepared by mixing the cathode active material (CAM) powders with conductive carbon (C65, Imerys Graphite & Carbon) and PVDF binder (Solef 5130,

Solvay GmbH) in a 94:3:3 mass ratio using a centrifugal planetary mixer (ARE 250, Thinky Corporation). The solid content of the final slurries was 61 wt %. The slurries were cast onto an Al-foil (thickness 20 μm, Nippon Light Metal Co., Ltd.) using a box-type coater (wet-film thickness 100 μm, width 6 cm, Erichsen GmbH & Co. KG) and an automated coating Table (5 mm s^{-1}, Coatmaster 510, Erichsen GmbH & Co. KG). The coated tapes were placed in a vacuum oven (VDL 23, Binder GmbH) and heated to 120 °C under vacuum for drying overnight. The dried cathode tapes were compressed using a calender (CA5, Sumet Systems GmbH) at a set line force of 30 N mm^{-1}.

Cell Assembly. CR2032 coin cells were assembled in an Ar-filled glovebox using a GF/D-type glass microfiber separator (Whatman), a 0.6 mm thick Li foil anode (Albemarle, Germany), and 95 μL of LP57 electrolyte (1 M $LiPF_6$ in 3:7 wt % ethylene carbonate:ethyl methyl carbonate, BASF SE). The positive caps, negative caps, and spacers of the coin cell casings were modified by electro-erosion for *operando* XRD experiments to have a central hole of diameter 5 mm and sealed with X-ray transparent glass windows of diameter 6 mm and thickness 160 μm using a surface-treated polyethylene foil.[48]

***Operando* XRD.** All cells were cycled at a specific current of 19 mA g^{-1} ($\approx$ C/10) using a Gamry Interface 1000 potentiostat. The degree of delithiation, x(Li), achieved during cycling was estimated based upon the measured charge (q [mAh]), the mass of the active material in the electrode (m [g]), and the theoretical capacity of each cathode material (q_{th} [mAh g^{-1}]), assuming a fully lithiated stoichiometry in the pristine electrode materials (i.e., initial value of x(Li) = 1) for the first charge cycle. XRD patterns were collected simultaneously using a STOE Stadi-P diffractometer with Mo anode. Diffraction data were collected in the range $5° < 2\theta < 37°$ with a collection time of 10 min per pattern. The zero offset and instrumental contribution to peak broadening were determined by measurement of a LaB_6 660b standard reference material.[49] Rietveld refinement was performed sequentially on the diffraction data using GSAS-II.[50] The use of a Mo anode ($\lambda_{Mo\,K\alpha}$ = 0.70926 Å) allows for a range of d-spacings ($d \approx$ 1.07−7.30 Å) to be measured, allowing the first 19 reflections from the cathode materials to be resolved. A compromise was achieved between intensity and time resolution by collecting patterns over a relatively small angular range ($5° < 2\theta < 37°$). This corresponds to ≈120 diffraction patterns per charge−discharge cycle or a Δx(Li) of ≈0.013 per pattern. All of the materials studied here are isostructural with α-$NaFeO_2$ and thus were modeled using a layered structure with space group $R\bar{3}m$. The site occupancies of the TM site (3*b*) in the structure were fixed to reflect the composition of the different cathode materials. Because of the poor sensitivity of XRD toward lithium, the site occupancy factor of the Li site (3*a*) was not refined during the sequential refinements. Similarly, the atomic displacement parameters (ADPs) of each site were fixed to established reasonable values previously determined in structural studies of transition-metal-based cathode materials.[51] Subtle differences in the relative intensity of reflections from the Al foil and Li foil counter electrode were observed between the different coin cells presented in this study due to the effects of preferred orientation, and so these phases were fitted using Pawley refinements using cubic structures with space group $Fm\bar{3}m$.[52] The cell parameters of the Li and Al phases were fixed to known values enabling the sample displacement of the coin cell stage to be accounted for. Size and strain broadening contributions of the layered phase, sample displacement parameters, and the background profile function were refined for the first pattern of each experiment and then fixed. A Chebyshev polynomial function with 23 terms was ascribed to the background profile. Parameters allowed to vary during the sequential refinement include the scale factor of each phase, the cell parameters, and the atomic coordinate of oxygen (z_{Ox}) in the electrochemically active layered phase. During sequential refinements the quality of fit R_{wp} was generally found to vary within ±3% during cycling (see Figure S1). An example of the quality of fit to the first pattern of each *operando* cycling experiment and the corresponding structural parameters are shown in Figure S2 and Table S1, respectively.

RESULTS AND DISCUSSION

To compare the consequences of Co or Mn substitution for structural evolution in Ni-rich materials, Figure 2 shows the evolution of diffraction data collected from coin cells containing cathode materials with identical Ni content, i.e., NiCo9010 ($LiNi_{0.9}Co_{0.1}O_2$) and NiMn9010 ($LiNi_{0.9}Mn_{0.1}O_2$), during the first charge−discharge cycle. Here, the Co-containing sample was cycled to an upper cutoff potential of 4.3 V, delivering a specific capacity of 232.5 mAh g^{-1}, while the Mn-containing sample was cycled to 4.5 V and delivered a virtually similar specific capacity of 237.6 mAh g^{-1}. The chosen cutoff potentials enable the two materials to reach a comparable lithium content of x(Li) ≈ 0.15 and 0.14, respectively.

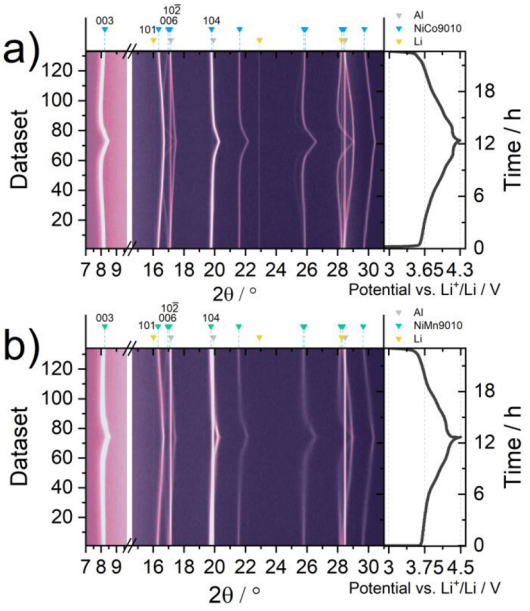

Figure 2. Contour maps of diffraction data collected during the first cycle of (a) NiCo9010 and (b) NiMn9010. Contour maps of diffraction data collected during the first cycle of all materials are shown in Figure S3.

Figure 3 shows the evolution of selected reflections of the NiMn9010 and NiCo9010 phases during the first cycle. The figure highlights the absence of any unfavorable phase transitions with 10% Ni substitution in the cathode regardless of whether this is realized with Co or Mn, in contrast to the purely ternary phases such as $LiNiO_2$ or $LiCoO_2$, when

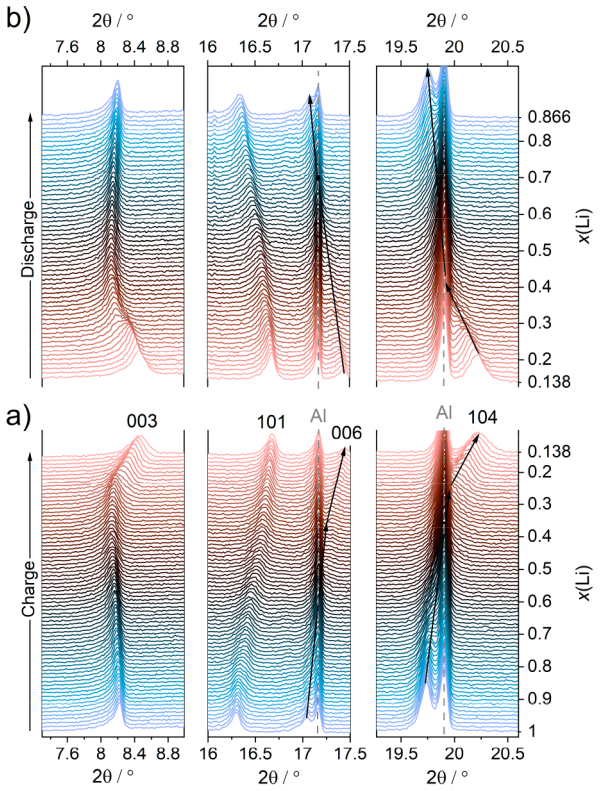

Figure 3. Stacked diffraction patterns highlighting selected angular regions collected during the (a) first charge cycle and (b) first discharge cycle of the cell containing NiMn9010.

subjected to comparable degrees of delithiation.[53−55] For example, a complex series of first-order phase transitions have been identified and well characterized during the delithiation of $LiNiO_2$.[56] Two-phase transitions have also been observed in Ni-rich NCA materials, for example, a distinct H2−H3 phase transition in $LiNi_{0.95}Co_{0.04}Al_{0.01}O_2$,[57] while an investigation of a series of quaternary Ni-rich materials ($LiNi_{0.95}M_{0.05}O_2$, with M = Al, Mn, Mg, and Co) showed that only Co substitution failed to suppress the phase transitions.[9] The 101 reflection correlates more with the change in the slab distance, *S*, which is depicted in Figure 1. This reflection is observed to initially behave in an opposite fashion to the others and shifts to higher angles, corresponding to the reduction in ionic radii of the TM sites as they are oxidized during delithiation. Meanwhile, the 003, 006, and 104 reflections originate from the alternating planes of Li and TM atoms in the layered structure, and thus their behavior can be related to expansion/contraction along the stacking axis. For example, during the delithiation of NiMn9010 (see Figure 3a), the 003 reflection is first observed to shift slowly to lower angles, corresponding to an expansion of the interlayer spacing of the cathode material structure. However, once the cell reaches 4.0 V, it then begins to rapidly shift to higher angles, corresponding to a significant decrease in the *c* lattice parameter as the material reaches high degrees of delithiation ($x(Li) < 0.3$). The initial expansion is attributed to increasing electrostatic repulsion between the transition-metal octahedra as lithium is removed from the structure. Lithium extraction from the structure occurs concurrently with TM oxidation, resulting in the transfer of negative charge from the octahedral oxygen atoms. Spectroscopic studies of Ni-rich cathodes have further confirmed the charge transfer from oxygen to highly oxidized Ni in the structure.[58] As a result, despite less screening between the repelling oxygen octahedra after lithium extraction, the reduced electron density at the oxygen positions allows for the contraction of the Li interslab distance as there is less repulsion between the opposite octahedra. This behavior leads to the observed structural collapse at deep states of charge[59] and is also common to various layered cathode materials.[60−67] Previous studies of NCM, in particular, have shown that the collapse is directly correlated to the degree of delithiation and not the chemical composition of the cathode material.[68,69] Upon discharge or during relithiation of the cathode (Figure 3b), the evolution of the reflections proceeds in the opposite fashion. Closer observation of the peak profiles of reflections at the beginning of discharge (Figure 3b) shows there is some broadening at high states of charge, particularly as the Li content progresses from $0.138 < x(Li) < 0.25$. This may be

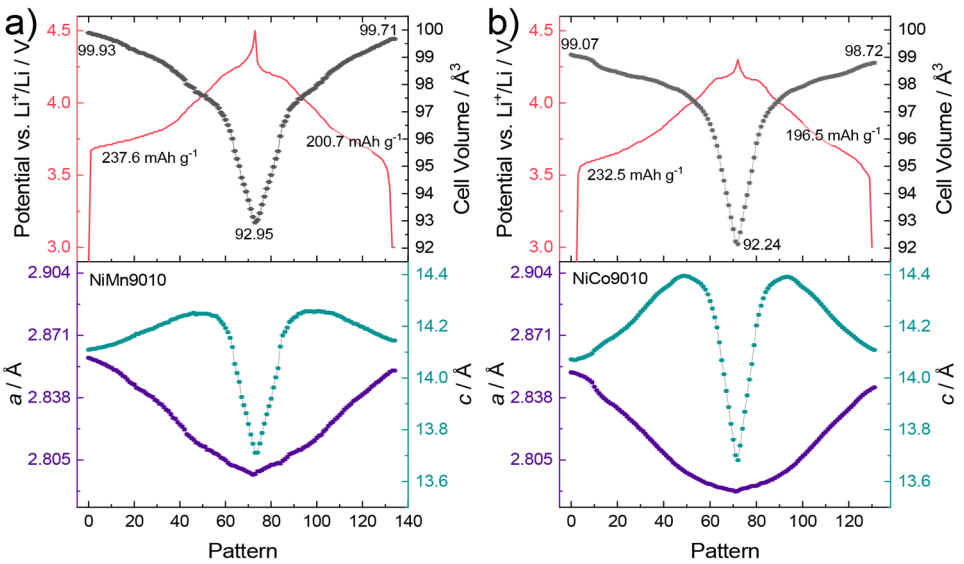

Figure 4. Refined unit cell parameters of the (a) NiMn9010 and (b) NiCo9010 materials during the first cycle.

Table 1. Refined Cell Parameters of NiMn9010 and NiCo9010 Observed at Various States of Charge during the First Charge–Discharge Cycle

	V/Å^3		a/Å		c/Å	
	NiMn9010	NiCo9010	NiMn9010	NiCo9010	NiMn9010	NiCo9010
initial	99.928(7)	99.067(5)	2.8596(2)	2.8512(1)	14.1109(8)	14.0716(5)
max					14.2523(16)	14.3936(7)
charged	92.952(11)	92.237(6)	2.7975(3)	2.7882(2)	13.7149(17)	13.7007(7)
discharged	99.710(9)	98.722(5)	2.8529(2)	2.8412(1)	14.1457(10)	14.1213(6)

related to phase segregation within the cathode material into Li-rich and Li-poor phases at high states of delithiation and at high current densities as a result of different Li diffusivity between the two phases.[70−72] This behavior has been previously observed in various Ni-rich materials with Ni content as low as $y = 0.6$ and thus could be expected to occur in all of the materials presented here.[73]

To compare and quantify the evolution of reflections observed in the diffraction data, Figure 4 shows the refined unit cell parameters of the NiMn9010 and NiCo9010 materials during the initial cycle, with identical axes used on both graphs. The quantitative evolution of lattice parameters was determined using sequential Rietveld refinements. It should be noted that several constraints were applied in the refinements as deemed appropriate for the sample environment and quality of the diffraction patterns. Further details can be found in the Experimental Section. When cycled to 4.5 and 4.3 V, respectively, it is evident that both materials undergo a very similar change in overall cell volume. The Co material, meanwhile, exhibits a much larger expansion and contraction along the c-axis compared to the Mn-containing material. Table 1 shows the range of cell parameters observed for each material during the first cycle. During the first cycle, the c lattice parameter of the NiMn9010 materials increases from the initial value of ≈14.11 to ≈14.25 Å at 4.0 V, before reducing to ≈13.71 Å as the cell reached the charged state at 4.5 V. In comparison, the c parameter of NiCo9010 begins at ≈14.07 Å and reaches a maximum value of ≈14.39 Å (at 3.98 V), before reducing to a minimum value of ≈13.7 Å at 4.3 V. This corresponds to a total c parameter variation ($[c_{max} - c_{min}]/c_{OCV}$) of ≈3.8% for NiMn9010 compared to ≈5.1% for NiCo9010. Meanwhile, in both materials the a lattice parameter undergoes a rather comparable continuous reduction as the electrode is delithiated. As lithium is removed, the transition-metal ions in the structure are oxidized to species with smaller ionic radii, e.g., Ni^{2+} (0.69 Å) → Ni^{3+} (0.56 Å) → Ni^{4+} (0.48 Å) or Co^{3+} (0.545 Å) → Co^{4+} (0.53 Å).[74] Thus, a decrease in the distance between adjacent transition-metal atoms in the structure, and therefore the a lattice parameter, is expected during delithiation.

Figure 5 shows the potential profiles and differential capacity curves recorded during the first cycle of the NiMn9010 and NiCo9010 materials. Considering first the potential profiles (Figure 5a), it is evident that the substitution of Mn for Co raises the average working voltage of the materials (≈3.82 V vs ≈3.93 V), indicated by a clear shift to higher potential on both charge and discharge, which should prove beneficial for energy density. Comparing the differential capacity curves (see Figure 5b), NiMn9010 exhibits a single peak at 3.7 V during charge, which corresponds to the Ni redox reaction, as Mn remains electrochemically inactive and retains a 4+ oxidation state throughout the measured potential window.[75,76] Meanwhile, the NiCo9010 curve shows additional features in this region,

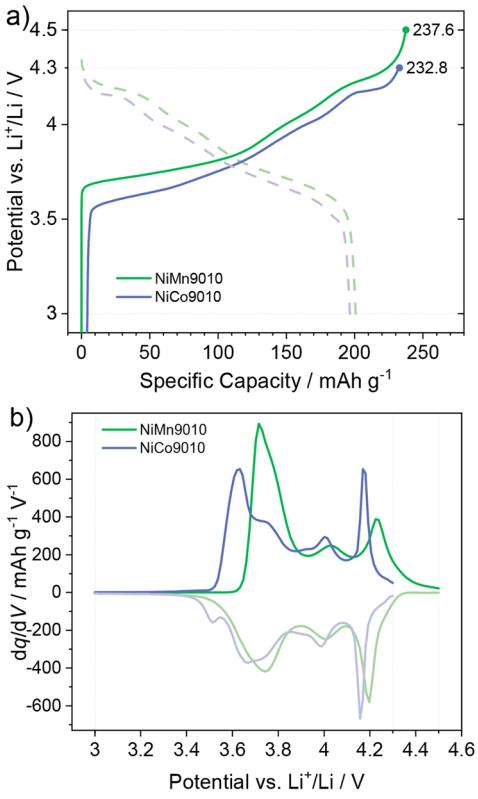

Figure 5. (a) Potential profiles recorded during the first cycle of NiMn9010 and NiCo9010 and (b) corresponding differential capacity curves.

corresponding to the overlapping redox activities of Ni and Co, with a peak already at 3.6 V.[77,78] At higher potential, both materials show a peak that is usually attributed to the H2−H3 transition in LNO/LCO materials, which occurs at ≈4.17 V for NiCo9010 but is observed at higher potentials ≈4.23 V for NiMn9010. Even though a first-order phase transition is not observed by XRD, its signature remains in the differential capacity curve. The shift in the potential at which the Ni redox features are observed can be attributed to the relative electronegativity of Ni/Mn or Ni/Co in these systems. Ni, Co, and Mn have tabulated electronegativities of $\chi_{Ni} = 1.91$, $\chi_{Co} = 1.88$, and $\chi_{Mn} = 1.55$, respectively.[79] Thus, the introduction of Co only weakly perturbates the neighboring Ni−O bonds. Conversely, introducing less electronegative Mn into the TM layer, whose bonding with the oxygen in surrounding octahedra is more ionic in nature than the neighboring Ni, leads to electrons that are localized closer to the oxygen p orbitals. This raises the potential required to induce the redox activity of Ni in the Ni−Mn system. This phenomenon has been described in analogy to the well-known "inductive effect" in polyanionic systems.[35,37] The interaction

of the completely occupied oxygen p orbitals with the partially filled d bands of the transition metals results in the formation of bonding and antibonding levels and, in particular, an increase in the energy of the e_g^* orbitals relative to the t_{2g} orbitals. The stronger the covalency of the TM−O bond, the greater the increase in energy of the antibonding orbitals. In Ni-rich cathode materials, where the Ni is involved in the redox reaction ($Ni^{2+} \leftrightarrow Ni^{3+} \leftrightarrow Ni^{4+}$), this will involve the exchange of electrons within these levels. Thus, if a different ion is substituted into an adjacent TM site in the structure, this will influence covalency of the Ni−O bonds in the TM octahedra and thereby also influence the potential at which the redox of Ni takes place.

Having established that the materials with 10 mol % Ni substitution both exhibit single-phase solid solution behavior when subjected to comparable degrees of delithiation, the effect of varying the Mn content among the materials was also investigated. Several $LiNi_{1-y}Mn_yO_2$ materials (y = 0.05−0.25) were cycled to varying upper cutoff potentials, and their observed potential profiles during the first cycle are shown in Figure 6a,b. Table 2 lists the observed capacities, lithium contents, and change in cell volume observed during the same cycle. As the Ni content in the active material is reduced, a higher upper cutoff potential is necessary to achieve a comparable capacity between the samples. This can be attributed to the fact that as the amount of Ni in the electrode is reduced, greater potentials are required to access the higher oxidation states of Ni ($Ni^{2+} \rightarrow Ni^{3+} \rightarrow Ni^{4+}$) and achieve comparable capacities. Interestingly, the required cutoff potential to achieve comparable Li utilization scales approximately linearly with the Ni content in the electrode (see Figure S4). As discussed earlier, the incorporation of Mn in the structure also promotes the reduction of Ni^{3+} during synthesis of the CAMs, making more Ni^{2+} available for redox during delithiation, which is why comparable capacities can still be attained despite the higher amount of electrochemically inactive Mn^{4+}.[80] This is reflected in the differential capacity curves of these materials (Figure 6c), where the characteristic redox features of each material are observed to shift to higher potentials with increasing Mn content on both charge and discharge, as expected from the earlier discussion.

Figure 7 shows the relative change of the cathode materials' a and c parameters during the first cycle, and absolute values are plotted in Figure S5. All of the materials studied here remain single phase throughout the entire cycle, including the NiMn9505 material. This shows that a small amount of Mn substitution is sufficient to suppress the first-order phase transitions typically observed during delithiation of $LiNiO_2$.[56] Comparing the evolution of lattice parameters as a function of potential (see Figure 7a,b), it is evident that there is negligible change in the cell parameters until 3.6 V for NiCo9010 and until 3.7 V for the Mn-containing materials. This is consistent with the first redox features observed in the dq/dV curves of these materials, discussed earlier and shown in Figures 5b and 6c. Meanwhile, monitoring the evolution of the a parameter as a function of lithium content (Figure 7c), it can be seen that it decreases roughly linearly from x(Li) ≈ 1 to 0.3 in all of the materials, which can be attributed to a decrease in the distance between adjacent transition-metal atoms in the structure as they are oxidized to species with smaller ionic radii. The overall change in a parameter ($\Delta a/a$) varies between ≈−2.01% and −2.15% for the Mn-containing materials (see Figure 8a). In contrast, the c lattice parameter initially increases as lithium is

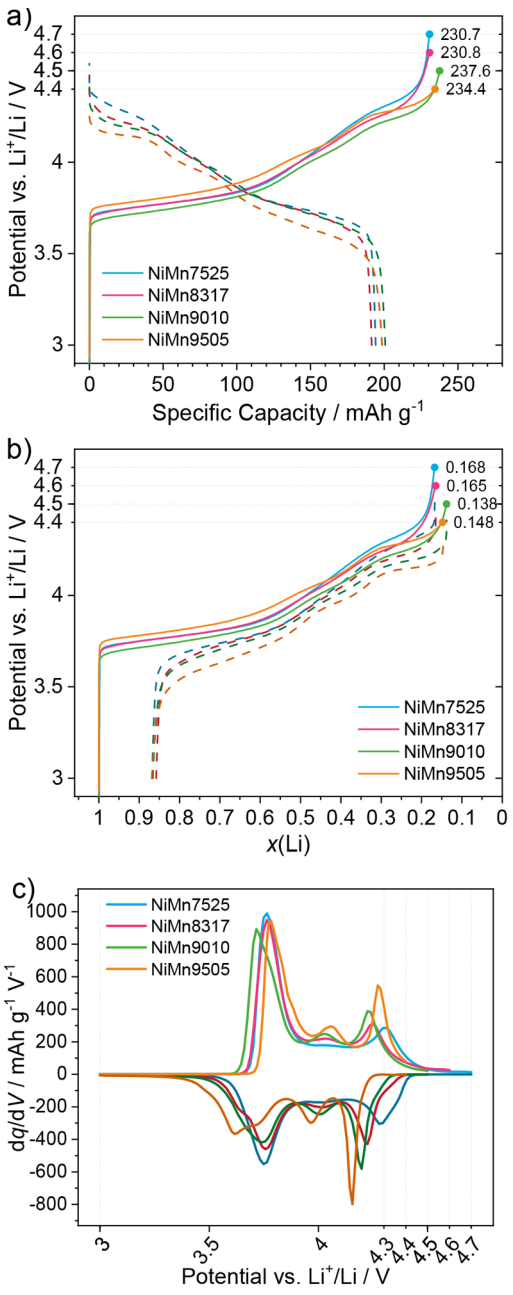

Figure 6. Potential profiles recorded during the first cycle of the $LiNi_{1-y}Mn_yO_2$ materials as a function of (a) specific capacity and (b) Li content. (c) Corresponding differential capacity curves.

removed from the structure. The removal of lithium exposes the layers of negatively charged oxygen octahedra to one another, and thus electrostatic repulsion causes the initial expansion. From Figure 7b,d, it is evident that the relative change in c parameter clearly varies as a function of the materials' compositions. Interestingly, the NiCo9010 material shows a much larger initial increase in c parameter (≈2.3%) compared to the $LiNi_{1-y}Mn_yO_2$ materials (≈1.0−1.3%). Among the latter materials, the overall change in c parameter grows larger with decreasing Mn content, from $\Delta c/c \approx -2.12\%$ in NiMn7525 to ≈ −3.83% in NiMn9505 (see Figure 8a). This decrease occurs despite comparable degrees of delithiation being achieved by the different materials, highlighting the role of Mn in mitigating the magnitude of structural change. This

Table 2. Measured Specific Capacities, Corresponding Lithium Content, and Change in Cell Volume of the $LiNi_{1-y}Mn_yO_2$ and $LiNi_{0.9}Co_{0.1}O_2$ Materials Observed during the First Cycle

	q/mAh g^{-1}		remaining x(Li)				
sample	1st charge	1st discharge	1st charge	1st discharge	Coulombic efficiency/%	Δcell vol/Å^3	Δcell vol/%
NiMn7525	230.72	194.13	0.1676	0.8680	84.1	−6.119(10)	−6.09
NiMn8317	230.80	191.49	0.1647	0.8577	83.0	−6.356(16)	−6.36
NiMn9010	237.60	200.71	0.1378	0.8661	84.5	−6.975(13)	−6.98
NiMn9505	234.63	198.51	0.1469	0.8687	84.6	−7.847(22)	−7.86
NiCo9010	232.79	196.53	0.1518	0.8679	84.4	−6.830(8)	−6.89

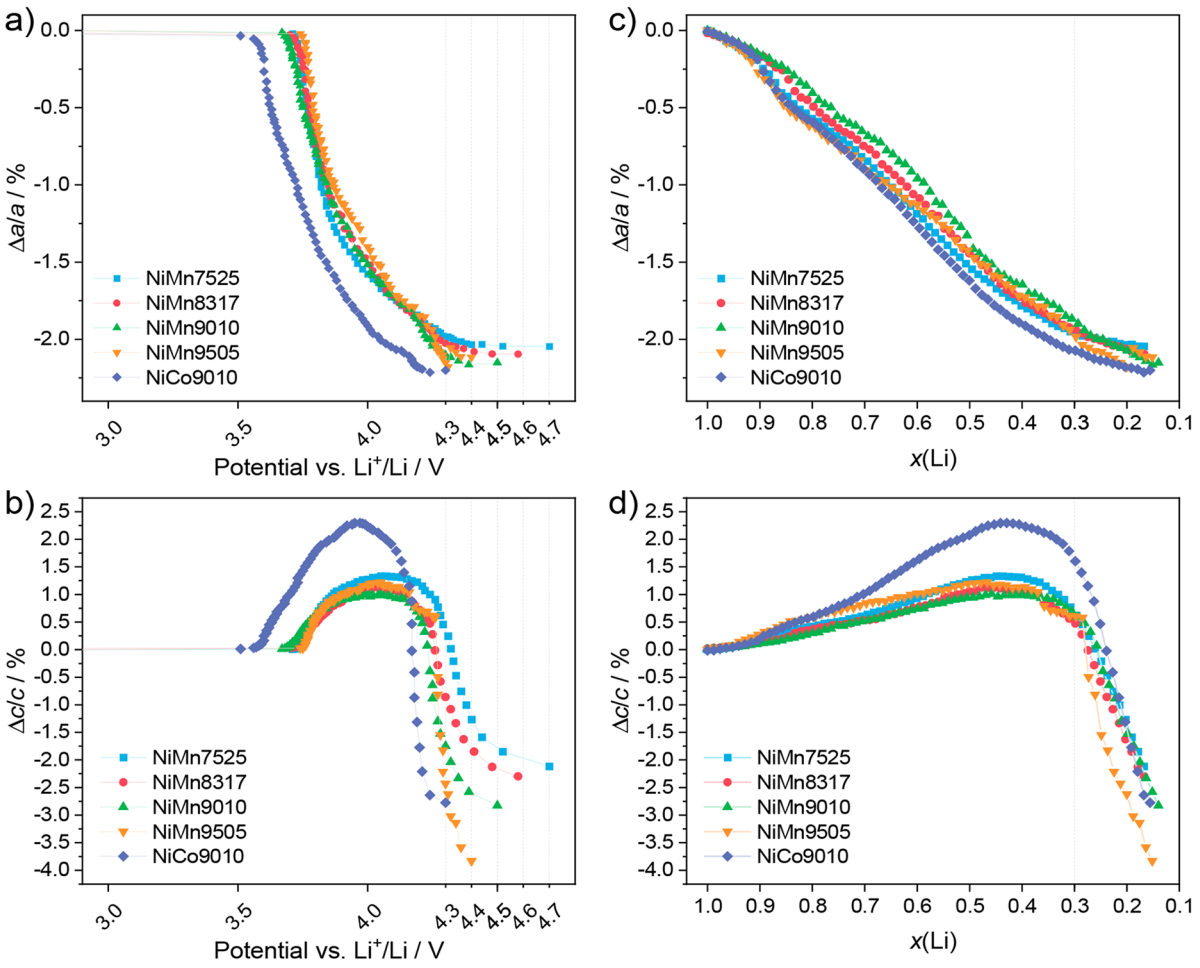

Figure 7. Relative changes in lattice parameters of the $LiNi_{1-y}Mn_yO_2$ and $LiNi_{0.9}Co_{0.1}O_2$ materials observed during the first charge (delithiation) as a function of (a, b) potential and (c, d) Li content.

figure also highlights that the anisotropy of the relative change in a and c parameters increases considerably as the Mn content in the cathode material is reduced. In fact, the relative changes in a and c parameters of NiMn7525 ($\Delta a/a \approx -2.05\%$ and $\Delta c/c \approx -2.12\%$) are quite similar, suggesting that the higher Mn content may also help to mitigate anisotropic volume variation among primary particles in the cathode material, thereby potentially preventing mechanical degradation of the electrode during cycling caused by cracking.[81,82] The anisotropy is visualized in Figure 8c by defining an "anisotropy index" calculated from the difference between the relative change in the a and c parameters. It is evident that all materials experience an anisotropic expansion during the initial delithiation ($1 > x(\mathrm{Li}) \geq 0.4$); however, the lattice collapse is clearly much more pronounced for the Ni-rich materials once the material is further delithiated. Considering the relative change in cell volume upon delithiation, shown in Figure 8b, a similar trend can be seen again where the absolute change reduces considerably with higher Mn content.

Figure 9a,b shows the evolution of the cathode materials' cell volume during the first cycle. As mentioned, the change in cell volume is attributed largely to the change in c parameter with increasing Ni content. Considering the evolution of cell volume as a function of potential, the materials initially undergo a sharp drop in volume at 3.7 V, before slowing and undergoing another sharp drop in volume after 4.2 V, in accordance with the "H1−M" and "H2−H3" redox features observed in the differential capacity curves presented earlier. However, considering the cell volume as a function of the materials state of delithiation, it can be seen that the cell

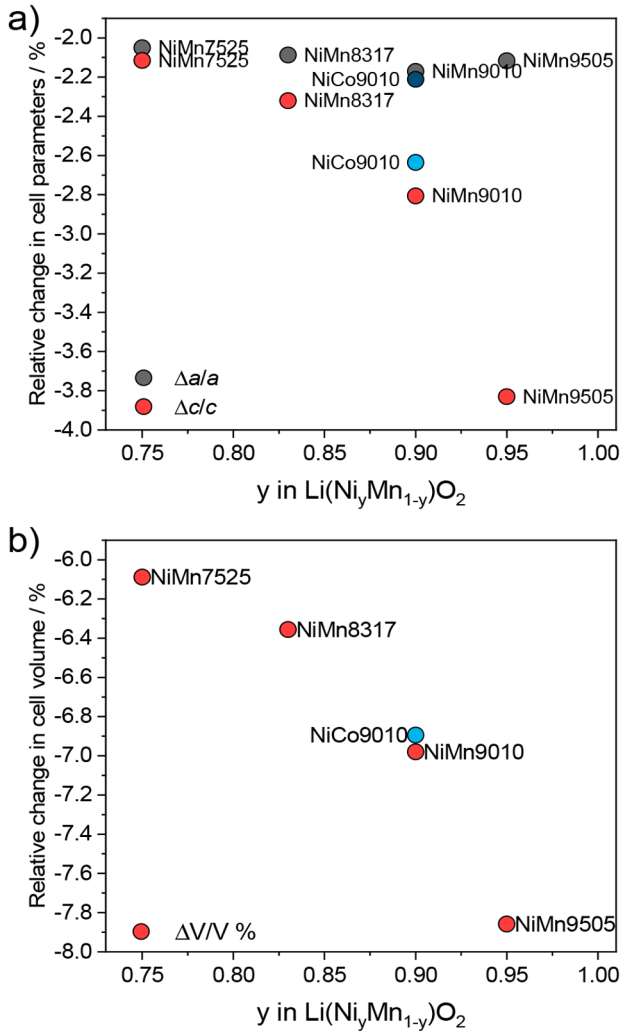

c

Figure 8. Relative change in (a) *a* and *c* lattice parameters and (b) in unit cell volume of the $LiNi_{1-y}Mn_yO_2$ and $LiNi_{0.9}Co_{0.1}O_2$ materials as a function of Ni content during the first charge (delithiation). (c) Evolution of the lattice anisotropy as a function of Li content in the electrode during the first charge (delithiation). Inset shows the maximum lattice anisotropy observed as a function of Ni content in the electrode.

volume initially decreases slowly due to the opposing contraction along the *a*-axis and expansion along the *c*-axis.

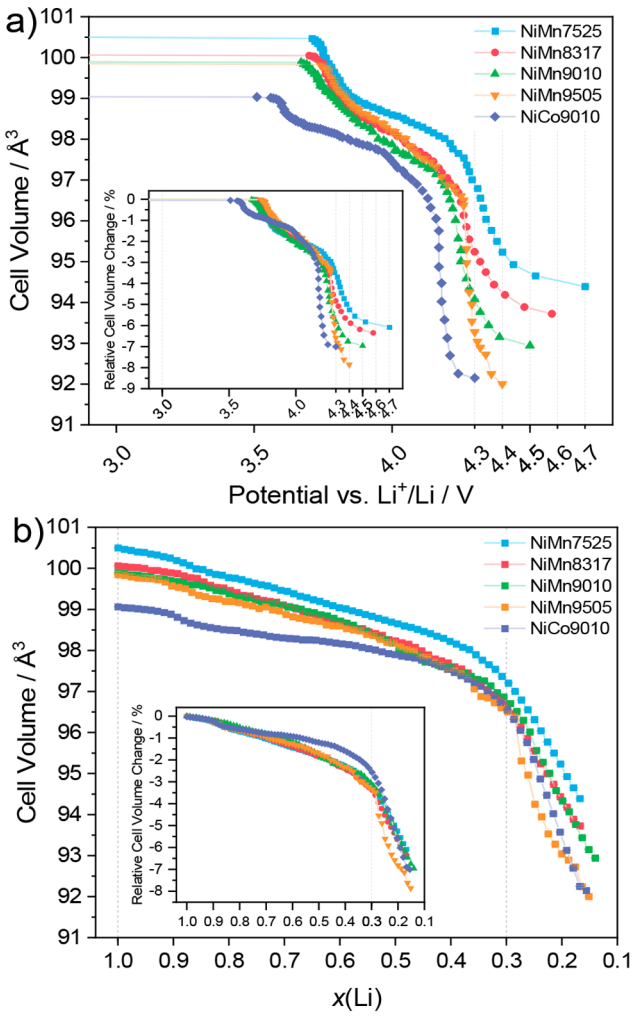

Figure 9. Refined cell volumes of the $LiNi_{1-y}Mn_yO_2$ and $LiNi_{0.9}Co_{0.1}O_2$ materials as a function of (a) potential and (b) Li content during the first charge (delithiation). Inset figures show the relative change in cell volume ($\Delta V/V/\%$).

This behavior continues until the Li content reaches $x(\mathrm{Li}) \approx 0.3$, beyond which a more pronounced reduction in cell volume begins.

The evolution of the atomic coordinate of oxygen (z_{Ox}), shown in Figure 10a, allows for the interlayer thickness (I) and TM layer thickness (S) of the cathode materials' structures to be calculated (Figure 10b,c). The evolution of this parameter is similar in all materials except NiMn7525, which shows a deviation once the Li content in the material reaches a value <0.3. I, which corresponds to the thickness of the Li slab, evolves in roughly the same fashion for all materials, and a gradual increase in the thickness is observed during delithiation, which can be attributed to the increasing repulsion between the opposing oxygen octahedra as Li is removed from the structure, until a collapse as the lithium content reduces below $x(\mathrm{Li}) \approx 0.3$, as discussed earlier. This preservation of the Li interslab distance is essential to the cyclability of layered positive electrodes, as it enables lithium diffusion pathways to be preserved and thus enables lithium to be reintercalated into the structure upon discharge.[59] S decreases gradually in all materials which reflects the reduction in ionic radii of the TMs upon oxidation during delithiation.

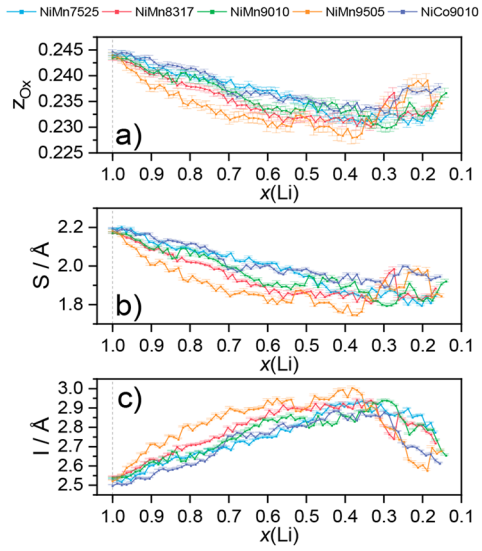

Figure 10. (a) Refined z coordinate of oxygen, (b) calculated layer thickness (S), and (c) calculated interlayer spacing (I) of the $LiNi_{1-y}Mn_yO_2$ and $LiNi_{0.9}Co_{0.1}O_2$ materials as a function of Li content during the first charge (delithiation). The Li site was defined as the origin (0, 0, 0) in the structural models refined against the diffraction data.

The structural evolution of the materials was also investigated during the second cycle, and observed electrochemical data and associated changes in cell volume are summarized in Table 3. The evolution of the structural parameters and recorded electrochemistry data can be found in the Supporting Information (see Figures S6 and S7). At the end of the first cycle, all materials return to a lithium content of $x(\mathrm{Li}) \approx 0.86$ (after discharge), suggesting the irreversible capacity loss on the first cycle is rather independent of the cathode material composition, and it is often more related to morphological and kinetic aspects.[83] Similarly to the first cycle, the materials are delithiated to a lithium content of $x(\mathrm{Li}) \approx 0.15-0.16$ when cycled to the previously defined upper cutoff potentials, and similar trends in the change of cell parameters and volume are observed in this cycle as well. During this cycle, all materials exhibit a comparable $\Delta a/a$ of $\approx -1.8-1.9\%$, while the relative change in c parameter is found to vary from $\Delta c/c \approx -2.3\%$ for NiMn7525 to -2.67% for NiMn9505.

OUTLOOK

The results presented above clearly demonstrate that by adjusting operating conditions to achieve comparable Li utilization, a representative comparison of the relationship between cathode material composition and structural evolution upon cycling can be made. Increasing the Mn content in Ni-rich, Co-free cathodes leads to improved structural stability while still providing comparable energy densities. In particular, the increased presence of electrochemically inert Mn also significantly reduces the magnitude of anisotropic volume expansion as the materials are delithiated. Such behavior could prove especially useful for application in solid-state batteries, where volume changes can cause contact loss between the active material and rigid solid electrolyte. However, it is important to consider that the choice of composition may have other implications for the materials' physical properties. Cobalt is highly beneficial for achieving good electronic conductivity in layered cathode materials, which is essential for achieving high rate capability, which is quickly becoming a practical necessity for applications requiring high power densities, such as electric vehicles.[84] The activation energy for Li diffusion is also lowest in LCO, while substitution with Ni or Mn increases the energy barrier to overcome.[85] This hindrance to conductivity is further exacerbated when Co-free materials are operated at lower temperatures.[86] Cobalt has also been associated with reduced cationic disorder in layered cathode materials, where mixing of Ni ions into the Li layer is expected to further hinder diffusion and lead to poor rate capability.[87] However, the migration of small amounts of Ni to the Li layer (1−3%) has recently been shown not to correlate with a reduction in capacity or irreversible capacity loss on the first cycle,[83] which may favor Mn-based Ni-rich materials. Another consideration for the choice of cathode material composition is the synthesis conditions, as Ni-rich materials are highly sensitive to synthesis temperature and also exhibit poor stability in uncontrolled atmospheres,[88] leading to the formation of residual lithium impurities at the surface of the materials, which adversely affects their electrochemical behavior.[89−91] Higher Ni contents require that the synthesis of the materials is performed in an oxygen atmosphere, as this promotes the oxidation of Ni^{2+} to Ni^{3+} and encourages lithium uptake.[92] Meanwhile, the substitution of Ni with other elements generally raises the temperature required for synthesis of the materials.[93−95] Thus, considerations about processing costs and physical properties must be made when promoting the performance of Ni-rich materials, as higher synthesis temperatures increase energy use, while conditions requiring controlled oxygen atmospheres and low humidity can also influence the scalability and cost of preparing these materials as well as their electrochemical behavior.

Although it was not observed here, it should also be considered that raising the operating voltage beyond 4.5 V, as required for the Mn-rich materials to achieve comparable

Table 3. Measured Specific Capacities, Corresponding Lithium Content, and Change in Cell Volume of the $LiNi_{1-y}Mn_yO_2$ and $LiNi_{0.9}Co_{0.1}O_2$ Materials Observed during the Second Cycle[a]

	q/mAh g^{-1}		remaining x(Li)				
sample	2nd charge	2nd discharge	2nd charge	2nd discharge	Coulombic efficiency/%	Δcell vol/Å^3	Δcell vol/%
NiMn7525	194.12	191.55	0.1678	0.8587	98.7	−5.688(11)	−5.68
NiMn8317	195.06	198.64	0.1518	0.8707	101.9	−6.241(13)	−6.26
NiMn9010	203.14	205.06	0.1291	0.8731	101.2	−6.797(17)	−6.82
NiMn9505	193.22	186.69	0.1662	0.8561	96.6	−6.405(26)	−6.41
NiCo9010	196.18	192.96	0.1531	0.8449	98.3	−6.570(7)	−6.66

[a]The lithium content and change in cell volume calculated for the second cycle were estimated using the final value after the first discharge as a starting point.

energy densities, may cause electrolyte decomposition.[96,97] The dissolution of TM ions was initially identified as an issue in the high-voltage operation of Mn-based spinels[98,99] but has since been shown to also occur in layered cathode materials.[100,101] This leads to accelerated decomposition of the electrolyte and growth of the insulating cathode electrolyte interphase (CEI)[102] or poisoning of the graphite SEI in full cells,[103] reducing the amount of available active material and leading to gradual capacity decay. Improvements to the structural stability and practical energy density of cathode materials should therefore not be considered in isolation, and further research will be required to optimize the entire LIB system to take advantage of these newly developed Ni-rich and/or Co-free cathode materials.

CONCLUSIONS

In this study the structural evolution in a series of Ni-rich, Co-free NMX ($LiNi_{1-y}Mn_yO_2$) cathode materials has been investigated by *operando* XRD. We demonstrate that the anisotropic volume variation diminishes significantly as the Mn content in the cathode material is increased. This reduction was achieved while ensuring all materials were subjected to comparable levels of delithiation, corroborating previous reports that the lattice collapse during delithiation is independent of the cathode composition and rather dependent on the amount of Li extraction. In addition, all materials investigated were found to exhibit largely single-phase solid solution behavior when cycled to a lithium content of $x(Li) \approx 0.15$. The anisotropy of the volume variation was observed to be significantly more pronounced with increasing Ni content. The structure−electrochemistry relationships observed during the delithiation of the materials presented in this study show that targeting Ni-rich materials with a higher Mn content, at the expense of Co, could be a promising path toward new cathode compositions with stable structural evolution and high capacity, while the substitution of Ni and Co with Mn would also reduce the cost of raw materials required. However, as discussed above, the complete elimination of Co may not be feasible for all applications as Co brings other beneficial material properties such as electronic conductivity over a wide range, particularly important for LIBs destined for electromobility applications.[86] Thus, Co-free NMX compositions may instead be more practical in lower cost applications where the cathode material does not limit the power density of the system. NMX materials could also hold promise for use in conjunction with solid electrolytes (SEs) because of the lower anisotropic volume changes, which may be beneficial to the chemomechanics of the system.[104] The use of novel halide SEs, which are stable over a wide electrochemical potential window,[105] could enable NMX-based systems with higher energy density and stable cycling by enabling operation at high voltage to achieve high Li utilization while avoiding chemical decomposition of the electrolyte, while the stable structural evolution helps to maintain contact between the CAM and SE. The data presented in this study highlight that these novel NMX cathodes can provide the energy densities expected of Ni-rich materials, while maintaining good mechanical stability achieved through reduced anisotropic volume variation, provided that considerations of full cell cycling stability are properly addressed.

ASSOCIATED CONTENT

Supporting Information

The Supporting Information is available free of charge at https://pubs.acs.org/doi/10.1021/acs.jpcc.2c04946.

Figures S1−S7 and Table S1 (PDF)

AUTHOR INFORMATION

Corresponding Author

Matteo Bianchini − *Battery and Electrochemistry Laboratory, Institute of Nanotechnology, Karlsruhe Institute of Technology (KIT), 76344 Eggenstein-Leopoldshafen, Germany; BASF SE, 67056 Ludwigshafen, Germany;* Present Address: University of Bayreuth and Bavarian Center for Battery Technology (BayBatt), Universitätsstrasse 30, 95447 Bayreuth, Germany; orcid.org/0000-0003-4034-7706; Email: matteo.bianchini@uni-bayreuth.de

Authors

Damian Goonetilleke − *Battery and Electrochemistry Laboratory, Institute of Nanotechnology, Karlsruhe Institute of Technology (KIT), 76344 Eggenstein-Leopoldshafen, Germany;* orcid.org/0000-0003-1033-4787

Felix Riewald − *Chair of Technical Electrochemistry, Department of Chemistry and Catalysis Research Center, Technical University of Munich, 85748 Garching, Germany; BASF SE, 67056 Ludwigshafen, Germany*

Aleksandr O. Kondrakov − *Battery and Electrochemistry Laboratory, Institute of Nanotechnology, Karlsruhe Institute of Technology (KIT), 76344 Eggenstein-Leopoldshafen, Germany; BASF SE, 67056 Ludwigshafen, Germany*

Jürgen Janek − *Battery and Electrochemistry Laboratory, Institute of Nanotechnology, Karlsruhe Institute of Technology (KIT), 76344 Eggenstein-Leopoldshafen, Germany; Institute of Physical Chemistry & Center for Materials Research (ZfM/LaMa), Justus-Liebig-University Giessen, 35392 Giessen, Germany;* orcid.org/0000-0002-9221-4756

Torsten Brezesinski − *Battery and Electrochemistry Laboratory, Institute of Nanotechnology, Karlsruhe Institute of Technology (KIT), 76344 Eggenstein-Leopoldshafen, Germany;* orcid.org/0000-0002-4336-263X

Notes

The authors declare no competing financial interest.

ACKNOWLEDGMENTS

This study was supported by BASF SE.

REFERENCES

(1) Ryu, H.-H.; Sun, H. H.; Myung, S.-T.; Yoon, C. S.; Sun, Y.-K. Reducing cobalt from lithium-ion batteries for the electric vehicle era. *Energy Environ. Sci.* **2021**, *14*, 844−852.

(2) Julien, C. M.; Mauger, A. NCA, NCM811, and the Route to Ni-Richer Lithium-Ion Batteries. *Energies* **2020**, *13* (23), 6363.

(3) Zhou, K.; Xie, Q.; Li, B. H.; Manthiram, A. An in-depth understanding of the effect of aluminum doping in high-nickel cathodes for lithium-ion batteries. *Energy Storage Materials* **2021**, *34*, 229−240.

(4) Grey, C. P.; Hall, D. S. Prospects for lithium-ion batteries and beyond-a 2030 vision. *Nat. Commun.* **2020**, *11* (1), 6279.

(5) Li, M.; Lu, J.; Chen, Z.; Amine, K. 30 Years of Lithium-Ion Batteries. *Adv. Mater.* **2018**, *30* (33), No. e1800561.
(6) Gourley, S. W. D.; Or, T.; Chen, Z. Breaking Free from Cobalt Reliance in Lithium-Ion Batteries. *iScience* **2020**, *23* (9), 101505.
(7) Sun, Y. K.; Lee, D. J.; Lee, Y. J.; Chen, Z.; Myung, S. T. Cobalt-free nickel rich layered oxide cathodes for lithium-ion batteries. *ACS Appl. Mater. Interfaces* **2013**, *5* (21), 11434−40.
(8) Luo, Y.-h.; Wei, H.-x.; Tang, L.-b.; Huang, Y.-d.; Wang, Z.-y.; He, Z.-j.; Yan, C.; Mao, J.; Dai, K.; Zheng, J.-c. Nickel-rich and cobalt-free layered oxide cathode materials for lithium ion batteries. *Energy Storage Materials* **2022**, *50*, 274−307.
(9) Li, H.; Cormier, M.; Zhang, N.; Inglis, J.; Li, J.; Dahn, J. R. Is Cobalt Needed in Ni-Rich Positive Electrode Materials for Lithium Ion Batteries? *J. Electrochem. Soc.* **2019**, *166* (4), A429−A439.
(10) Cui, Z.; Xie, Q.; Manthiram, A. A Cobalt- and Manganese-Free High-Nickel Layered Oxide Cathode for Long-Life, Safer Lithium-Ion Batteries. *Adv. En. Mater.* **2021**, *11* (41), 2102421.
(11) Muralidharan, N.; Essehli, R.; Hermann, R. P.; Parejiya, A.; Amin, R.; Bai, Y.; Du, Z.; Belharouak, I. LiNixFeyAlzO2, a new cobalt-free layered cathode material for advanced Li-ion batteries. *J. Power Sources* **2020**, *471*, 228389.
(12) Yi, M.; Li, W.; Manthiram, A. Delineating the Roles of Mn, Al, and Co by Comparing Three Layered Oxide Cathodes with the Same Nickel Content of 70% for Lithium-Ion Batteries. *Chem. Mater.* **2022**, *34* (2), 629−642.
(13) Delmas, C.; Fouassier, C.; Hagenmuller, P. Structural classification and properties of the layered oxides. *Physica B+ C* **1980**, *99* (1−4), 81−85.
(14) Bianchini, M.; Roca-Ayats, M.; Hartmann, P.; Brezesinski, T.; Janek, J. There and Back Again—The Journey of LiNiO2 as a Cathode Active Material. *Angew. Chem., Int. Ed.* **2019**, *58*, 10434−10458.
(15) Tian, Z.; Yu, H.; Zhang, Z.; Xu, X. Performance Improvements of Cobalt Oxide Cathodes for Rechargeable Lithium Batteries. *ChemBioEng. Reviews* **2018**, *5* (2), 111−118.
(16) Mizushima, K.; Jones, P.; Wiseman, P.; Goodenough, J. B. LixCoO2 (0< x<-1): A new cathode material for batteries of high energy density. *Mater. Res. Bull.* **1980**, *15* (6), 783−789.
(17) Zhao, H.; Lam, W. Y. A.; Sheng, L.; Wang, L.; Bai, P.; Yang, Y.; Ren, D.; Xu, H.; He, X. Cobalt-Free Cathode Materials: Families and their Prospects. *Adv. Energy Mater.* **2022**, DOI: 10.1002/aenm.202103894.
(18) Stansby, J. H.; Sharma, N.; Goonetilleke, D. Probing the charged state of layered positive electrodes in sodium-ion batteries: reaction pathways, stability and opportunities. *J. Mater. Chem. A* **2020**, *8*, 24833−24867.
(19) Manthiram, A. A reflection on lithium-ion battery cathode chemistry. *Nat. Commun.* **2020**, *11* (1), 1550.
(20) Ong, S. P.; Chevrier, V. L.; Hautier, G.; Jain, A.; Moore, C.; Kim, S.; Ma, X.; Ceder, G. Voltage, stability and diffusion barrier differences between sodium-ion and lithium-ion intercalation materials. *Energy Environ. Sci.* **2011**, *4* (9), 3680−3688.
(21) Tuccillo, M.; Palumbo, O.; Pavone, M.; Muñoz-García, A. B.; Paolone, A.; Brutti, S. Analysis of the Phase Stability of LiMO2 Layered Oxides (M = Co, Mn, Ni). *Crystals* **2020**, *10* (6), 526.
(22) Zhang, Y.; Xie, H.; Jin, H.; Zhang, Q.; Li, Y.; Li, X.; Li, K.; Bao, C. Research Status of Spinel LiMn2O4 Cathode Materials for Lithium Ion Batteries. *IOP Conference Series: Earth and Environmental Science* **2020**, *603* (1), 012051.
(23) Thackeray, M. M.; Amine, K. LiMn2O4 spinel and substituted cathodes. *Nature Energy* **2021**, *6* (5), 566−566.
(24) Armstrong, A. R.; Bruce, P. G. Synthesis of layered LiMnO2 as an electrode for rechargeable lithium batteries. *Nature* **1996**, *381* (6582), 499−500.
(25) Capitaine, F.; Gravereau, P.; Delmas, C. A new variety of LiMnO2 with a layered structure. *Solid State Ionics* **1996**, *89* (3−4), 197−202.
(26) Shao-Horn, Y.; Hackney, S.; Armstrong, A.; Bruce, P.; Gitzendanner, R.; Johnson, C.; Thackeray, M. Structural characterization of layered LiMnO2 electrodes by electron diffraction and lattice imaging. *J. Electrochem. Soc.* **1999**, *146* (7), 2404.
(27) Vitins, G.; West, K. Lithium Intercalation into Layered LiMnO2. *J. Electrochem. Soc.* **1997**, *144* (8), 2587−2592.
(28) Bruce, P. G.; Armstrong, A. R.; Gitzendanner, R. L. New intercalation compounds for lithium batteries: layered LiMnO 2. *J. Mater. Chem.* **1999**, *9* (1), 193−198.
(29) Nishi, Y. Lithium ion secondary batteries; past 10 years and the future. *J. Power Sources* **2001**, *100* (1−2), 101−106.
(30) Yoon, C. S.; Jun, D. W.; Myung, S. T.; Sun, Y. K. Structural Stability of LiNiO2 Cycled above 4.2 V. *Acs Energy Letters* **2017**, *2* (5), 1150−1155.
(31) Liu, Q.; Su, X.; Lei, D.; Qin, Y.; Wen, J.; Guo, F.; Wu, Y. A.; Rong, Y.; Kou, R.; Xiao, X.; Aguesse, F.; Bareño, J.; Ren, Y.; Lu, W.; Li, Y. Approaching the capacity limit of lithium cobalt oxide in lithium ion batteries via lanthanum and aluminium doping. *Nature Energy* **2018**, *3* (11), 936−943.
(32) Shao-Horn, Y.; Levasseur, S.; Weill, F.; Delmas, C. Probing Lithium and Vacancy Ordering in O3 Layered Li[sub x]CoO[sub 2] (x≈0.5). *J. Electrochem. Soc.* **2003**, *150* (3), A366.
(33) Yang, J. H.; Kim, H.; Ceder, G. Insights into Layered Oxide Cathodes for Rechargeable Batteries. *Molecules* **2021**, *26* (11), 3173.
(34) Liu, C.; Neale, Z. G.; Cao, G. Understanding electrochemical potentials of cathode materials in rechargeable batteries. *Mater. Today* **2016**, *19* (2), 109−123.
(35) Meng, Y. S.; Arroyo-de Dompablo, M. E. Recent Advances in First Principles Computational Research of Cathode Materials for Lithium-Ion Batteries. *Acc. Chem. Res.* **2013**, *46* (5), 1171−1180.
(36) Padhi, A. K.; Manivannan, V.; Goodenough, J. B. Tuning the Position of the Redox Couples in Materials with NASICON Structure by Anionic Substitution. *J. Electrochem. Soc.* **1998**, *145* (5), 1518−1520.
(37) Goodenough, J. B. Bond-Length Mismatch in Intergrowth Structures. *J. Less-Common Met.* **1986**, *116* (1), 83−93.
(38) Goonetilleke, D.; Stansby, J. H.; Sharma, N. In situ studies: electrochemistry and scattering. *Current Opinion in Electrochemistry* **2019**, *15*, 18−26.
(39) Strauss, F.; Kitsche, D.; Ma, Y.; Teo, J. H.; Goonetilleke, D.; Janek, J.; Bianchini, M.; Brezesinski, T. Operando Characterization Techniques for All-Solid-State Lithium-Ion Batteries. *Advanced Energy and Sustainability Research* **2021**, *2* (6), 2100004.
(40) Aiken, C. P.; Xia, J.; Wang, D. Y.; Stevens, D. A.; Trussler, S.; Dahn, J. R. An Apparatus for the Study of In Situ Gas Evolution in Li-Ion Pouch Cells. *J. Electrochem. Soc.* **2014**, *161* (10), A1548−A1554.
(41) Harks, P.; Mulder, F.; Notten, P. In situ methods for Li-ion battery research: A review of recent developments. *J. Power Sources* **2015**, *288*, 92−105.
(42) Peterson, V. K.; Papadakis, C. M. Functional materials analysis using in situ and in operando X-ray and neutron scattering. *IUCrJ.* **2015**, *2* (2), 292−304.
(43) Senyshyn, A.; Mühlbauer, M. J.; Dolotko, O.; Hofmann, M.; Pirling, T.; Ehrenberg, H. Spatially resolved in operando neutron scattering studies on Li-ion batteries. *J. Power Sources* **2014**, *245*, 678−683.
(44) Wu, J.; Fenech, M.; Webster, R. F.; Tilley, R. D.; Sharma, N. Electron microscopy and its role in advanced lithium-ion battery research. *Sustainable Energy & Fuels* **2019**, *3*, 1623−1646.
(45) Liang, G. M.; Hao, J. N.; D'Angelo, A. M.; Peterson, V. K.; Guo, Z. P.; Pang, W. K. A Robust Coin-Cell Design for In Situ Synchrotron-based X-Ray Powder Diffraction Analysis of Battery Materials. *Batteries & Supercaps* **2021**, *4* (2), 380−384.
(46) Herklotz, M.; Scheiba, F.; Hinterstein, M.; Nikolowski, K.; Knapp, M.; Dippel, A.-C.; Giebeler, L.; Eckert, J.; Ehrenberg, H. Advances in in situ powder diffraction of battery materials: a case study of the new beamline P02.1 at DESY, Hamburg. *J. Appl. Crystallogr.* **2013**, *46* (4), 1117−1127.
(47) Zhang, L.; Guo, X.; Huang, J.; Qu, Y.; Niu, C.; Du, Z.; Li, D.; Chen, Y. Coin-cell-Based In Situ characterization Techniques for li-ion Batteries. *Frontiers in Energy Research* **2018**, *6*, 16.

(48) Herklotz, M.; Weiss, J.; Ahrens, E.; Yavuz, M.; Mereacre, L.; Kiziltas-Yavuz, N.; Drager, C.; Ehrenberg, H.; Eckert, J.; Fauth, F.; Giebeler, L.; Knapp, M. A novel high-throughput setup for in situ powder diffraction on coin cell batteries. *J. Appl. Crystallogr.* **2016**, *49* (1), 340−345.
(49) Black, D. R.; Windover, D.; Henins, A.; Filliben, J.; Cline, J. P. Certification of standard reference material 660B. *Powder Diffr.* **2011**, *26* (2), 155−158.
(50) Toby, B. H.; Von Dreele, R. B. GSAS-II: the genesis of a modern open-source all purpose crystallography software package. *J. Appl. Crystallogr.* **2013**, *46* (2), 544−549.
(51) Yin, L.; Mattei, G. S.; Li, Z.; Zheng, J.; Zhao, W.; Omenya, F.; Fang, C.; Li, W.; Li, J.; Xie, Q.; Zhang, J. G.; Whittingham, M. S.; Meng, Y. S.; Manthiram, A.; Khalifah, P. G. Extending the limits of powder diffraction analysis: Diffraction parameter space, occupancy defects, and atomic form factors. *Rev. Sci. Instrum.* **2018**, *89* (9), 093002.
(52) Wyckoff, R. W. G. *Crystal Structures*; Interscience: New York, 1963; Vol. *1*.
(53) Duffiet, M.; Blangero, M.; Cabelguen, P. E.; Delmas, C.; Carlier, D. Influence of the Initial Li/Co Ratio in LiCoO2 on the High-Voltage Phase-Transitions Mechanisms. *J. Phys. Chem. Lett.* **2018**, *9* (18), 5334−5338.
(54) Manthiram, A.; Choi, J.; Choi, W. Factors limiting the electrochemical performance of oxide cathodes. *Solid State Ionics* **2006**, *177* (26), 2629−2634.
(55) Chen, Z.; Lu, Z.; Dahn, J. R. Staging Phase Transitions in Li x CoO2. *J. Electrochem. Soc.* **2002**, *149* (12), A1604−A1609.
(56) Li, H. Y.; Zhang, N.; Li, J.; Dahn, J. R. Updating the Structure and Electrochemistry of LixNiO2 for $0 \leq x \leq 1$. *J. Electrochem. Soc.* **2018**, *165* (13), A2985−A2993.
(57) Nam, G. W.; Park, N.-Y.; Park, K.-J.; Yang, J.; Liu, J.; Yoon, C. S.; Sun, Y.-K. Capacity Fading of Ni-Rich NCA Cathodes: Effect of Microcracking Extent. *ACS Energy Lett.* **2019**, *4* (12), 2995−3001.
(58) Kondrakov, A. O.; Geßwein, H.; Galdina, K.; de Biasi, L.; Meded, V.; Filatova, E. O.; Schumacher, G.; Wenzel, W.; Hartmann, P.; Brezesinski, T.; Janek, J. Charge-Transfer-Induced Lattice Collapse in Ni-Rich NCM Cathode Materials during Delithiation. *J. Phys. Chem. C* **2017**, *121* (44), 24381−24388.
(59) Lee, W.; Muhammad, S.; Kim, T.; Kim, H.; Lee, E.; Jeong, M.; Son, S.; Ryou, J. H.; Yoon, W. S. New insight into Ni-rich layered structure for next-generation Li rechargeable batteries. *Adv. En. Mater.* **2018**, *8* (4), 1701788.
(60) Bak, S.-M.; Hu, E.; Zhou, Y.; Yu, X.; Senanayake, S. D.; Cho, S.-J.; Kim, K.-B.; Chung, K. Y.; Yang, X.-Q.; Nam, K.-W. Structural Changes and Thermal Stability of Charged LiNixMnyCozO2 Cathode Materials Studied by Combined In Situ Time-Resolved XRD and Mass Spectroscopy. *ACS Appl. Mater. Interfaces* **2014**, *6* (24), 22594−22601.
(61) Goonetilleke, D.; Sharma, N.; Pang, W. K.; Peterson, V. K.; Petibon, R.; Li, J.; Dahn, J. R. Structural Evolution and High-Voltage Structural Stability of Li(NixMnyCoz)O2 Electrodes. *Chem. Mater.* **2019**, *31* (2), 376−386.
(62) Tapia-Ruiz, N.; Dose, W. M.; Sharma, N.; Chen, H.; Heath, J.; Somerville, J. W.; Maitra, U.; Islam, M. S.; Bruce, P. G. High voltage structural evolution and enhanced Na-ion diffusion in P2-Na2/3Ni1/3-xMgxMn2/3O2 ($0 \leq x \leq 0.2$) cathodes from diffraction, electrochemical and ab initio studies. *Energy Environ. Sci.* **2018**, *11* (6), 1470−1479.
(63) Reimers, J. N.; Dahn, J. R. Electrochemical and In Situ X-Ray Diffraction Studies of Lithium Intercalation in Li x CoO2. *J. Electrochem. Soc.* **1992**, *139* (8), 2091−2097.
(64) Amatucci, G.; Tarascon, J.; Klein, L. Coo2, the end member of the li x coo2 solid solution. *J. Electrochem. Soc.* **1996**, *143* (3), 1114−1123.
(65) Lu, Z.; Dahn, J. In Situ X-Ray Diffraction Study of P 2 Na2/3 [Ni1/3Mn2/3] O 2. *J. Electrochem. Soc.* **2001**, *148* (11), A1225−A1229.
(66) Li, J.; Petibon, R.; Glazier, S.; Sharma, N.; Pang, W. K.; Peterson, V. K.; Dahn, J. R. In-situ Neutron Diffraction Study of a High Voltage Li(Ni0.42Mn0.42Co0.16)O2/Graphite Pouch Cell. *Electrochim. Acta* **2015**, *180*, 234−240.
(67) Li, W.; Reimers, J.; Dahn, J. In situ x-ray diffraction and electrochemical studies of Li1- xNiO2. *Solid State Ionics* **1993**, *67* (1−2), 123−130.
(68) Li, W.; Asl, H. Y.; Xie, Q.; Manthiram, A. Collapse of LiNi1- x-yCo xMn yO2 Lattice at Deep Charge Irrespective of Nickel Content in Lithium-Ion Batteries. *J. Am. Chem. Soc.* **2019**, *141* (13), 5097−5101.
(69) Li, H.; Liu, A.; Zhang, N.; Wang, Y.; Yin, S.; Wu, H.; Dahn, J. R. An Unavoidable Challenge for Ni-Rich Positive Electrode Materials for Lithium-Ion Batteries. *Chem. Mater.* **2019**, *31* (18), 7574−7583.
(70) Nomura, Y.; Yamamoto, K.; Yamagishi, Y.; Igaki, E. Lithium Transport Pathways Guided by Grain Architectures in Ni-Rich Layered Cathodes. *ACS Nano* **2021**, *15* (12), 19806−19814.
(71) Lim, J.-M.; Hwang, T.; Kim, D.; Park, M.-S.; Cho, K.; Cho, M. Intrinsic origins of crack generation in Ni-rich LiNi0. 8Co0. 1Mn0. 1O2 layered oxide cathode material. *Sci. Rep.* **2017**, *7* (1), 1−10.
(72) Goonetilleke, D.; Wang, S.; Gonzalo, E.; Galcerán, M.; Saurel, D.; Day, S. J.; Fauth, F.; Rojo, T.; Sharma, N. Exploring the rate dependence of phase evolution in P2-type Na2/3Mn0.8Fe0.1-Ti0.1O2. *J. Mater. Chem. A* **2019**, *7* (19), 12115−12125.
(73) Hyun, H.; Jeong, K.; Hong, H.; Seo, S.; Koo, B.; Lee, D.; Choi, S.; Jo, S.; Jung, K.; Cho, H. H.; Han, H. N.; Shin, T. J.; Lim, J. Suppressing High-Current-Induced Phase Separation in Ni-Rich Layered Oxides by Electrochemically Manipulating Dynamic Lithium Distribution. *Adv. Mater.* **2021**, *33* (51), No. e2105337.
(74) Shannon, R. D. Revised Effective Ionic-Radii and Systematic Studies of Interatomic Distances in Halides and Chalcogenides. *Acta Crystallogr., Sect. A* **1976**, *32* (Sep1), 751−767.
(75) Breddemann, U.; Sicklinger, J.; Schipper, F.; Davis, V.; Fischer, A.; Huber, K.; Erickson, E. M.; Daub, M.; Hoffmann, A.; Erk, C.; Markovsky, B.; Aurbach, D.; Gasteiger, H. A.; Krossing, I. Fluorination of Ni-Rich Lithium-Ion Battery Cathode Materials by Fluorine Gas: Chemistry, Characterization, and Electrochemical Performance in Full-cells. *Batteries & Supercaps* **2021**, *4* (4), 632−645.
(76) Xiao, J.; Chernova, N. A.; Whittingham, M. S. Layered Mixed Transition Metal Oxide Cathodes with Reduced Cobalt Content for Lithium Ion Batteries. *Chem. Mater.* **2008**, *20* (24), 7454−7464.
(77) Delmas, C.; Saadoune, I.; Rougier, A. The cycling properties of the LixNi1- yCoyO2 electrode. *J. Power Sources* **1993**, *44* (1−3), 595−602.
(78) Ohzuku, T.; Ueda, A. Phenomenological Expression of Solid-State Redox Potentials of LiCoO2, LiCo1/2Ni1/2 O 2, and LiNiO2 Insertion Electrodes. *J. Electrochem. Soc.* **1997**, *144* (8), 2780−2785.
(79) Tantardini, C.; Oganov, A. R. Thermochemical electronegativities of the elements. *Nat. Commun.* **2021**, *12* (1), 2087.
(80) Kim, D.; Lim, J.-M.; Lim, Y.-G.; Yu, J.-S.; Park, M.-S.; Cho, M.; Cho, K. Design of Nickel-rich Layered Oxides Using d Electronic Donor for Redox Reactions. *Chem. Mater.* **2015**, *27* (18), 6450−6456.
(81) Kondrakov, A. O.; Schmidt, A.; Xu, J.; Geßwein, H.; Mönig, R.; Hartmann, P.; Sommer, H.; Brezesinski, T.; Janek, J. Anisotropic Lattice Strain and Mechanical Degradation of High- and Low-Nickel NCM Cathode Materials for Li-Ion Batteries. *J. Phys. Chem. C* **2017**, *121* (6), 3286−3294.
(82) Chen, J.; Yang, H.; Li, T.; Liu, C.; Tong, H.; Chen, J.; Liu, Z.; Xia, L.; Chen, Z.; Duan, J.; Li, L. The Effects of Reversibility of H2-H3 Phase Transition on Ni-Rich Layered Oxide Cathode for High-Energy Lithium-Ion Batteries. *Front Chem.* **2019**, *7*, 500.
(83) Riewald, F.; Kurzhals, P.; Bianchini, M.; Sommer, H.; Janek, J.; Gasteiger, H. The LiNiO2 Cathode Active Material: A Comprehensive Study of Calcination Conditions and their Correlation with Physicochemical Properties Part II. Morphology. *J. Electrochem. Soc.* **2022**, *169* (2), 020529.
(84) Weiss, M.; Ruess, R.; Kasnatscheew, J.; Levartovsky, Y.; Levy, N. R.; Minnmann, P.; Stolz, L.; Waldmann, T.; Wohlfahrt-Mehrens,

M.; Aurbach, D.; Winter, M.; Ein-Eli, Y.; Janek, J. Fast Charging of Lithium-Ion Batteries: A Review of Materials Aspects. *Adv. En. Mater.* **2021**, *11* (33), 2101126.
(85) Luo, G.; Zhao, J.; Ke, X.; Zhang, P.; Sun, H.; Wang, B. Structure, Electrode Voltage and Activation Energy of LiMnxCoyNi1-x-yO2Solid Solutions as Cathode Materials for Li Batteries from First-Principles. *J. Electrochem. Soc.* **2012**, *159* (8), A1203−A1208.
(86) Ryu, H.-H.; Kang, G.-C.; Ismoyojati, R.; Park, G.-T.; Maglia, F.; Sun, Y.-K. Intrinsic weaknesses of Co-free Ni-Mn layered cathodes for electric vehicles. *Mater. Today* **2022**, *56*, 8−15.
(87) Zheng, J.; Ye, Y.; Liu, T.; Xiao, Y.; Wang, C.; Wang, F.; Pan, F. Ni/Li Disordering in Layered Transition Metal Oxide: Electrochemical Impact, Origin, and Control. *Acc. Chem. Res.* **2019**, *52* (8), 2201−2209.
(88) Liu, H. S.; Zhang, Z. R.; Gong, Z. L.; Yang, Y. Origin of Deterioration for LiNiO2 Cathode Material during Storage in Air. *Electrochem. Solid-State Lett.* **2004**, *7* (7), A190.
(89) Jung, R.; Morasch, R.; Karayaylali, P.; Phillips, K.; Maglia, F.; Stinner, C.; Shao-Horn, Y.; Gasteiger, H. A. Effect of Ambient Storage on the Degradation of Ni-Rich Positive Electrode Materials (NMC811) for Li-Ion Batteries. *J. Electrochem. Soc.* **2018**, *165* (2), A132−A141.
(90) Lin, Y.; Xu, M.; Tian, Y.; Fan, W.; Yu, L.; Li, W. Understanding impacts of environmental relative humidity to the cell performance based on LiNi0. 8Co0. 15Al0. 05O2 cathode. *Mater. Chem. Phys.* **2018**, *211*, 200−205.
(91) Faenza, N. V.; Bruce, L.; Lebens-Higgins, Z. W.; Plitz, I.; Pereira, N.; Piper, L. F. J.; Amatucci, G. G. Growth of Ambient Induced Surface Impurity Species on Layered Positive Electrode Materials and Impact on Electrochemical Performance. *J. Electrochem. Soc.* **2017**, *164* (14), A3727−A3741.
(92) Liu, A.; Phattharasupakun, N.; Väli, R.; Ouyang, D.; Dahn, J. R. Tracking the Fate of Excess Li in the Synthesis of Various Liy[Ni1-xMnx]O2 Positive Electrode Materials Under Different Atmospheres. *J. Electrochem. Soc.* **2022**, *169* (3), 030538.
(93) Ronduda, H.; Zybert, M.; Szczesna-Chrzan, A.; Trzeciak, T.; Ostrowski, A.; Szymanski, D.; Wieczorek, W.; Rarog-Pilecka, W.; Marcinek, M. On the Sensitivity of the Ni-rich Layered Cathode Materials for Li-ion Batteries to the Different Calcination Conditions. *Nanomaterials (Basel)* **2020**, *10* (10), 2018.
(94) Zheng, J.; Yan, P.; Estevez, L.; Wang, C.; Zhang, J.-G. Effect of calcination temperature on the electrochemical properties of nickel-rich LiNi0. 76Mn0. 14Co0. 10O2 cathodes for lithium-ion batteries. *Nano Energy* **2018**, *49*, 538−548.
(95) Habibi, A.; Jalaly, M.; Rahmanifard, R.; Ghorbanzadeh, M. The effect of calcination conditions on the crystal growth and battery performance of nanocrystalline Li (Ni 1/3 Co 1/3 Mn 1/3) O 2 as a cathode material for Li-ion batteries. *New J. Chem.* **2018**, *42* (23), 19026−19033.
(96) Strauss, F.; Teo, J. H.; Schiele, A.; Bartsch, T.; Hatsukade, T.; Hartmann, P.; Janek, J.; Brezesinski, T. Gas Evolution in Lithium-Ion Batteries: Solid versus Liquid Electrolyte. *ACS Appl. Mater. Interfaces* **2020**, *12* (18), 20462−20468.
(97) Li, M.; Wang, C.; Chen, Z.; Xu, K.; Lu, J. New Concepts in Electrolytes. *Chem. Rev.* **2020**, *120* (14), 6783−6819.
(98) Du Pasquier, A.; Blyr, A.; Courjal, P.; Larcher, D.; Amatucci, G.; Gérand, B.; Tarascon, J. M. Mechanism for Limited 55°C Storage Performance of Li1.05Mn1.95 O 4 Electrodes. *J. Electrochem. Soc.* **1999**, *146* (2), 428−436.
(99) Yang, L.; Takahashi, M.; Wang, B. A study on capacity fading of lithium-ion battery with manganese spinel positive electrode during cycling. *Electrochim. Acta* **2006**, *51* (16), 3228−3234.
(100) Jung, R.; Linsenmann, F.; Thomas, R.; Wandt, J.; Solchenbach, S.; Maglia, F.; Stinner, C.; Tromp, M.; Gasteiger, H. A. Nickel, Manganese, and Cobalt Dissolution from Ni-Rich NMC and Their Effects on NMC622-Graphite Cells. *J. Electrochem. Soc.* **2019**, *166* (2), A378−A389.
(101) Wandt, J.; Freiberg, A.; Thomas, R.; Gorlin, Y.; Siebel, A.; Jung, R.; Gasteiger, H. A.; Tromp, M. Transition metal dissolution and deposition in Li-ion batteries investigated by operando X-ray absorption spectroscopy. *J. Mater. Chem. A* **2016**, *4* (47), 18300−18305.
(102) Liu, W.; Li, J.; Li, W.; Xu, H.; Zhang, C.; Qiu, X. Inhibition of transition metals dissolution in cobalt-free cathode with ultrathin robust interphase in concentrated electrolyte. *Nat. Commun.* **2020**, *11* (1), 3629.
(103) Wang, A.; Kadam, S.; Li, H.; Shi, S.; Qi, Y. Review on modeling of the anode solid electrolyte interphase (SEI) for lithium-ion batteries. *npj Comput. Mater.* **2018**, *4* (1), 15.
(104) Minnmann, P.; Strauss, F.; Bielefeld, A.; Ruess, R.; Adelhelm, P.; Burkhardt, S.; Dreyer, S. L.; Trevisanello, E.; Ehrenberg, H.; Brezesinski, T.; Richter, F. H.; Janek, J. Designing Cathodes and Cathode Active Materials for Solid-State Batteries. *Adv. Energy Mater.* **2022**, *12* (35), 2201425.
(105) Zhou, L.; Zuo, T.-T.; Kwok, C. Y.; Kim, S. Y.; Assoud, A.; Zhang, Q.; Janek, J.; Nazar, L. F. High areal capacity, long cycle life 4 V ceramic all-solid-state Li-ion batteries enabled by chloride solid electrolytes. *Nature Energy* **2022**, *7* (1), 83−93.